2016
International Symposium on Power Electronics,
Electrical Drives, Automation and Motion

A 3-D Analytical Model of a Halbach Axial Magnetic Coupling

Kang Li
Electrical and Computer Engineering Department
University of North Carolina at Charlotte
Charlotte, NC, USA
kli10@uncc.edu

Jonathan Z. Bird
Electrical and Computer Engineering Department
Portland State University
Portland, OR, USA
jonathan.bird@ieee.org

***Abstract*—A 3-D analytical model is presented for a Halbach axial magnetic coupling. The field and torque are determined by first solving a 2-D field problem at the radial location in which the radial flux density is assumed zero. The solution to the 2-D problem is then incorporated into a 3-D magnetic charge sheet model so as to enable the complete 3-D fields and torque to be accurately computed. The presented model is compared with a 3-D finite element analysis model. The new 3-D field and torque analysis approach can be extended to model other 3-D axial magnetic devices.**

Keywords—axial coupling; magnetic charge; Halbach rotor

I. Introduction

A permanent magnetic coupling (PMC) provides a means of spatially transmitting torque without physical contact. It enables components to be isolated and thereby can minimize or eliminate mechanical vibration through magnetic damping [1]. A PMC can act as a torque limiter that can isolate loads when subjected to over torque conditions [2]. A PMC also allows one to insert a mechanical barrier between the drivers allowing torque to be transmitted between separate environments under different pressure differentials [3].

As the PMC is capable of continuously operating at a high sustained magnetic shear stress the study of the mass and volumetric torque densities of PMCs provides insight into the upper performance bound at which other magnetic devices, such as magnetic gearboxes [4, 5] are able to achieve.

There are two main types of PMCs, axial and radial topologies [6]. This paper focuses on deriving exact closed form 3-D torque and field equations for an axial Halbach rotor coupling. The fields in an axial magnetic coupling (AMC) are highly dependent on radial position and therefore in order to accurately model the field profile and consequently torque a full 3-D model is needed. Lubin *et. al.* [7, 8] demonstrated that if only 2-D AMC models are used the error can be up to 30% [7, 8].

Wang *et. al.* [9], Shin *et. al.* [10] and Yao *et. al.* [11] utilized the 3-D finite element analysis (FEA) method to study the performance of an AMC. While Dolisy *et. al.* created a 3-D analytic model of a magnetic coupling by ignoring the curvature effects [12, 13]. This approach was shown to be quite accurate when the air-gap is not large. Furlani [14] and Waring *et. al.* [15] computed the 3-D field and torque due to two magnetic rotor couplings surrounded by air. In order to create the model the field contributions were discretized by subdividing the individual segments into magnetic charge regions and then summing up the contributions of each surface. Such an approach is highly accurate [11, 14] but the approach is laborious and the final equation is hard to interpret. Furlani's formula results in the need to evaluate a torque expression that contains six embedded summation terms [14]. Such an approach cannot be extended to problems that contain magnetic steel. Thompson *et. al.* [16, 17] used a similar approach. Thompson derived the 3-D field for an axial Halbach rotor by summing up the individual field contributions from individual surface current sheets on each magnet surface. This approach required the evaluation of many double integrals as well as summation terms and the approach also cannot be generalized to model problems that contain magnetic steel.

This paper presents a different type of analytic approach to that presented previously [7, 8, 12-17]. In this paper the 3-D field and consequently torque created by a Halbach AMC is determined by using two primary steps:

(a) The axial field for one rotor is solved in 2-D at radius

$$r_c = (r_o + r_i)/2 \tag{1}$$

(b) The field solution from (a) is then used as the magnetic charge source term for an equivalent magnetic charge disc model. The equations are then solved using an integral approach.

By following the above two steps it is shown in this paper that highly accurate 3-D field and torque equations for a magnetic coupling can be determined. The resulting torque equation is easy to compute as it only needs one integral to be evaluated. Although the approach presented here is for a Halbach AMC the presented approach could be extended to model AMCs that contain magnetic steel [7, 8, 12, 13].

II. 2-D Analytical Model

The model of an axial Halbach rotor is shown in Fig. 1. It has an inner radius, r_i, an outer radius, r_o and an axial length d_I. The rotor magnets are magnetized along the axial direction as shown. The field created by the Halbach rotor is first solved at radius r_c. It is assumed that at radius r_c the radial field is

978-1-5090-2067-6/16/$31.00 ©2016 IEEE

zero (due to symmetry). Therefore at $r=r_c$ the magnetic field is assumed to be fully described by

$$\mathbf{B}(r_c,\theta,z) = 0\hat{\mathbf{r}} + B_\theta(r_c,\theta,z)\hat{\boldsymbol{\theta}} + B_z(r_c,\theta,z)\hat{\mathbf{z}} \quad (2)$$

Therefore the field **B** will exist only on a 2-D cylindrical surface as illustrated in Fig. 2. Surface regions Ω_I and Ω_{III} are non-magnetic regions and surface region Ω_{II} contains the axial magnetized Halbach magnets. By solving for the field in this 2-D model the magnetic charge value necessary to model the 3-D field can be obtained (as discussed in section III).

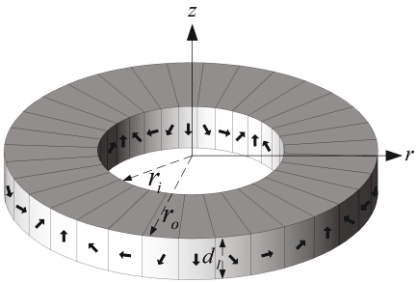

Fig. 1. An axial Halbach rotor.

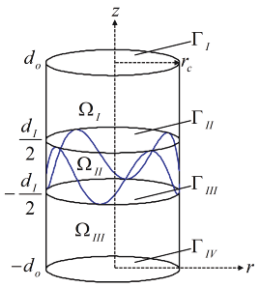

Fig. 2. The 2-D cylinderical surface region for the 2-D analytical model.

A. Governing Equations

Maxwell's equations for a magnetostatic current-free problem are given by [18]:

$$\nabla\cdot\mathbf{B} = 0 \quad (3)$$

$$\nabla\times\mathbf{H} = 0 \quad (4)$$

The constitutive equation when a magnetization vector **M** is presented is given by:

$$\mathbf{B} = \mu_0\mu_r\mathbf{H} + \mu_0\mathbf{M} \quad (5)$$

Substituting (5) into (3) and assuming linearity gives

$$\mu_r\nabla\cdot\mathbf{H} = -\nabla\cdot\mathbf{M} \quad (6)$$

From (4) the magnetic field intensity is related to the magnetic scalar potential by

$$\mathbf{H} = -\nabla\phi \quad (7)$$

Therefore

$$H_\theta = -\frac{1}{r_c}\frac{\partial\phi}{\partial\theta} \quad (8)$$

$$H_z = -\frac{\partial\phi}{\partial z} \quad (9)$$

Substituting (7) into (6) yields

$$\frac{1}{r_c^2}\frac{\partial^2\phi^{II}}{\partial\theta^2} + \frac{\partial^2\phi^{II}}{\partial z^2} = \frac{\nabla\cdot\mathbf{M}}{\mu_r}, \text{ in } \Omega_{II} \quad (10)$$

In the non-magnetic regions **M** = 0 and so (10) becomes:

$$\frac{1}{r_c^2}\frac{\partial^2\phi^{I}}{\partial\theta^2} + \frac{\partial^2\phi^{I}}{\partial z^2} = 0, \text{ in } \Omega_I \quad (11)$$

$$\frac{1}{r_c^2}\frac{\partial^2\phi^{III}}{\partial\theta^2} + \frac{\partial^2\phi^{III}}{\partial z^2} = 0, \text{ in } \Omega_{III} \quad (12)$$

B. Magnetization Vector

The magnetizing distribution in region Ω_{II} can be expressed by the Fourier series

$$\mathbf{M} = M_z(\theta)\hat{\mathbf{z}} + M_\theta(\theta)\hat{\boldsymbol{\theta}} \quad (13)$$

$$= \sum_{n=1}^{\infty} a_n\cos(np_I\theta)\hat{\mathbf{z}} + \sum_{n=1}^{\infty} b_n\sin(np_I\theta)\hat{\boldsymbol{\theta}} \quad (14)$$

where

$$a_n = \frac{4}{T}\int_0^{\pi/p_I} M_z(\theta)\cos(np_I\theta)d\theta \quad (15)$$

$$b_n = \frac{4}{T}\int_0^{\pi/p_I} M_\theta(\theta)\sin(np_I\theta)d\theta \quad (16)$$

and p_I = pole-pairs, $T=2\pi/p_I$. The Halbach rotor is made up three different magnet types: (1) axially magnetized (2) angular magnetized and (3) angular and axially magnetized magnets. Type (3) magnets are modeled using a superposition of type (1) and (2) magnets. This is illustrated in Fig. 3.

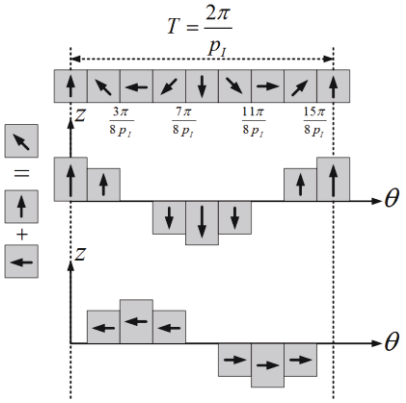

Fig. 3. The superposition of M_z and M_θ Halbach magnetized magnets.

Referring to Fig. 3 equation (15) can be written as:

$$a_n = \frac{4}{T}\left[\int_0^{\frac{\pi}{8p_I}} M\cos(np_I\theta)d\theta + \int_{\frac{\pi}{8p_I}}^{\frac{3\pi}{8p_I}} \frac{\sqrt{2}}{2}M\cos(np_I\theta)d\theta - \int_{\frac{5\pi}{8p_I}}^{\frac{7\pi}{8p_I}} \frac{\sqrt{2}}{2}M\cos(np_I\theta)d\theta - \int_{\frac{7\pi}{8p_I}}^{\frac{\pi}{p_I}} M\cos(np_I\theta)d\theta\right] \quad (17)$$

where $M = B_r/\mu_o$ and B_r = residual magnetic flux density. Such an approximation was used by Xia *et al.* [19] and provides an accurate result when the Halbach magnets are highly segmented. Evaluating (17) and simplifying yields:

$$a_n = \frac{2M}{n\pi}\sin(n\frac{\pi}{2})[(2-\sqrt{2})\cos(n\frac{3\pi}{8}) + \sqrt{2}\cos(n\frac{\pi}{8})] \quad (18)$$

Similarly evaluating (16) one obtains:

$$b_n = a_n\sin(n\pi/2) \quad (19)$$

Therefore $|a_n|=|b_n|$. Substituting (19) into (14) gives

$$\mathbf{M} = \sum_{n=1}^{\infty} a_n[\cos(np_I\theta)\hat{\mathbf{z}} + \sin(n\frac{\pi}{2})\sin(np_I\theta)\hat{\boldsymbol{\theta}}] \quad (20)$$

The harmonics terms for the case when p_I = 4 are shown in Fig. 4. The fundamental has the magnitude of

$$|a_1| = c_1M = c_1B_r/\mu_o \quad (21)$$

where c_1 = 0.9745. If only the fundamental is considered then after substituting (20) into (10) and utilizing (21) one obtains

$$\frac{1}{r_c^2}\frac{\partial^2\phi^{II}}{\partial\theta^2}+\frac{\partial^2\phi^{II}}{\partial z^2}=-p_1\frac{c_1B_r}{\mu_o\mu_r r_c}\cos(p_1\theta),\ \text{in}\ \Omega_{II} \quad (22)$$

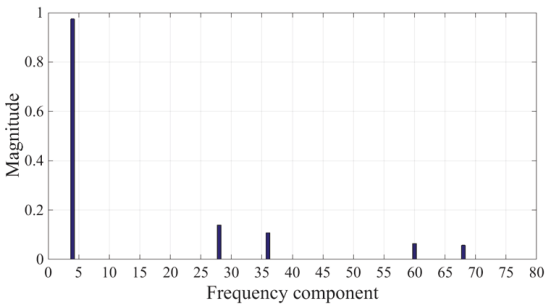

Fig. 4. Magnitude of different harmonics

C. Boundary Conditions

The boundary conditions at Γ_{II} are given by:

$$\left.\frac{\partial\phi^{I}(\theta,z)}{\partial z}\right|_{z=\frac{d_1}{2}}=\left.\frac{\mu_r\partial\phi^{II}(\theta,z)}{\partial z}\right|_{z=\frac{d_1}{2}}-\frac{c_1B_r\cos(p_1\theta)}{\mu_0} \quad (23)$$

$$\left.\frac{\partial\phi^{I}(\theta,z)}{\partial\theta}\right|_{z=\frac{d_1}{2}}=\left.\frac{\partial\phi^{II}(\theta,z)}{\partial\theta}\right|_{z=\frac{d_1}{2}} \quad (24)$$

and the boundary conditions at Γ_{III} are given by:

$$\left.\frac{\mu_r\partial\phi^{II}(\theta,z)}{\partial z}\right|_{z=-\frac{d_1}{2}}-\frac{c_1B_r\cos(p_1\theta)}{\mu_0}=\left.\frac{\partial\phi^{III}(\theta,z)}{\partial z}\right|_{z=-\frac{d_1}{2}} \quad (25)$$

$$\left.\frac{\partial\phi^{II}(\theta,z)}{\partial\theta}\right|_{z=-\frac{d_1}{2}}=\left.\frac{\partial\phi^{III}(\theta,z)}{\partial\theta}\right|_{z=-\frac{d_1}{2}} \quad (26)$$

The outer boundaries at $\pm d_o$ are assumed to be sufficiently far away such that

$$H_\theta^{\ I}(\theta,d_o)=0 \quad (27)$$

$$H_\theta^{\ III}(\theta,-d_o)=0 \quad (28)$$

D. General Solution

By using the separation of variables method, the general solution to (11) and (12) are:

$$\phi^{I}(r_c,\theta,z)=C\cos(p_1\theta)e^{-\frac{p_1}{r_c}(z-\frac{d_1}{2})} \quad (29)$$

$$\phi^{III}(r_c,\theta,z)=G\cos(p_1\theta)e^{\frac{p_1}{r_c}(z+\frac{d_1}{2})} \quad (30)$$

where C and G are unknowns that need to be determined.

The general solution of (22) is obtained by determining the homogeneous and particular solution of (22). By using the superposition principal one obtains [20]

$$\phi^{II}(r_c,\theta,z)=[\frac{r_cc_1B_r}{\mu_r\mu_o p_1}+De^{\frac{p_1}{r_c}\left(z+\frac{d_1}{2}\right)}+Fe^{\frac{-p_1}{r_c}\left(z-\frac{d_1}{2}\right)}]\cos(p_1\theta) \quad (31)$$

where D and F are unknowns that need to be determined

Substituting (29)-(31) into (23)-(26) enables the four unknown terms in (29)-(31) to be determined as

$$C=\frac{2c_1B_rr_c}{\mu_o p_1}\frac{e^{k_1}(\mu_r+1)(e^{k_1}-e^{-k_1})}{[e^{2k_1}(\mu_r+1)^2-e^{-2k_1}(\mu_r-1)^2]} \quad (32)$$

$$G=\frac{2c_1B_rr_c}{\mu_0 p_1}\frac{e^{-k_1}(\mu_r-1)(e^{k_1}-e^{-k_1})}{[e^{2k_1}(\mu_r+1)^2-e^{-2k_1}(\mu_r-1)^2]} \quad (33)$$

$$D=\frac{c_1B_rr_c}{\mu_0\mu_r p_1}\frac{e^{-k_1}(\mu_r^{\ 2}-1)(e^{k_1}-e^{-k_1})}{\left[e^{2k_1}(\mu_r+1)^2-e^{-2k_1}(\mu_r-1)^2\right]} \quad (34)$$

$$F=\frac{c_1B_rr_c}{\mu_0\mu_r p_1}\frac{e^{-k_1}\left[e^{-k_1}(\mu_r-1)^2-e^{k_1}(\mu_r+1)^2\right]}{\left[e^{2k_1}(\mu_r+1)^2-e^{-2k_1}(\mu_r-1)^2\right]} \quad (35)$$

where

$$k_1=p_1\frac{d_1}{2r_c}=p_1\frac{d_1}{r_o+r_i} \quad (36)$$

Substituting (32) into (29) and utilizing (8)-(9) gives:

$$\mathbf{B}^I(r_c,\theta,z)=B_m^I\left[\sin(p_1\theta)\hat{\boldsymbol{\theta}}+\cos(p_1\theta)\hat{\mathbf{z}}\right]e^{\frac{-p_1}{r_c}\left(z-\frac{d_1}{2}\right)} \quad (37)$$

where

$$B_m^I=2c_1B_r\frac{(\mu_r+1)e^{k_1}(e^{k_1}-e^{-k_1})}{e^{2k_1}(\mu_r+1)^2-e^{-2k_1}(\mu_r-1)^2} \quad (38)$$

III. 3-D Analytical Model

The 2-D model in the previous section does not consider the radial length of the rotor. To take into account the field variation along the radial length a magnetic charge disc is utilized. The charge disc has inner radius r_i and outer radius r_o as shown in Fig. 5. The disc is located axially at $z_1 = d_1/2$.

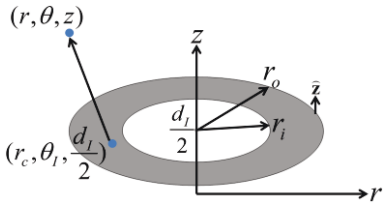

Fig. 5. 3-D axial charge disc model. The magnetic charge is only present between r_i and r_o.

A. General Solution

The magnetic scalar potential due to the surface magnetic charge disc can be computed from

$$\phi(r,\theta,z)=\frac{1}{4\pi\mu_0}\int_0^{2\pi}\int_{r_i}^{r_o}\frac{\rho_m(\theta_1)}{R_1}r_c\,dr_c\,d\theta_1 \quad (39)$$

where

$$R_1(r_c,z_1)=\sqrt{r^2+r_c^{\ 2}-2rr_c\cos(\theta-\theta_1)+(z-z_1)^2} \quad (40)$$

and the charge distributed over the disc is described by charge function $\rho_m(\theta_1)$. Substituting (39) into (7) the magnetic flux density created by the magnetic charge sheet disc is:

$$\mathbf{B}(r,\theta,z)=\frac{1}{4\pi}\int_0^{2\pi}\int_{r_i}^{r_o}\frac{\rho_m(\theta_1)\mathbf{R}}{R_1^3}r_c\,dr_c\,d\theta_1 \quad (41)$$

where

$$\mathbf{R}=\left[r-r_c\cos(\theta-\theta_1)\right]\hat{\mathbf{r}}+\left[r_c\sin(\theta-\theta_1)\right]\hat{\boldsymbol{\theta}}+(z-d_1/2)\hat{\mathbf{z}} \quad (42)$$

B. Charge Function

The boundary interface condition at the location of the charge sheet is defined as [18]

$$\rho_m(\theta_I) = (\mathbf{B}^I - \mathbf{B}^{II}) \cdot \hat{\mathbf{z}} \tag{43}$$

where superscripts *I* and *II* denote the field terms just above and below the magnetic charge sheet respectively. As all the external field emanates normally from the charge sheet the field above and below the charge disc, at the boundary, must be equal and opposite:

$$\mathbf{B}^{II} \cdot \hat{\mathbf{z}} = -\mathbf{B}^{I} \cdot \hat{\mathbf{z}} \tag{44}$$

Substituting (44) into (43) gives [21]

$$\rho_m(\theta_I) = 2\mathbf{B}^I(r_c, \theta, d_I/2) \cdot \hat{\mathbf{z}} \tag{45}$$

From (37) the value of B_z^I at $(r,\theta,z) = (r_c,\theta,d_I/2)$ is defined. Substituting (37) into (45) gives

$$\rho_m(\theta_I) = 2B_m^I \cos(p_I\theta_I) \tag{46}$$

The magnitude value in (46) is assumed constant across the surface of the charge disc.

C. Field Solution

Substituting (46) and (42) into (41) gives the magnetic flux density field values as

$$B_r^I(r,\theta,z) = \frac{B_m^I}{2\pi}\int_0^{2\pi}\int_{r_i}^{r_o} \frac{r_c}{R_1^3}[r - r_c\cos(\theta-\theta_I)]\cos(p_I\theta_I)dr_c d\theta_I \tag{47}$$

$$B_\theta^I(r,\theta,z) = \frac{B_m^I}{2\pi}\int_0^{2\pi}\int_{r_i}^{r_o} \frac{r_c^2}{R_1^3}\sin(\theta-\theta_I)\cos(p_I\theta_I)dr_c d\theta_I \tag{48}$$

$$B_z^I(r,\theta,z) = \frac{B_m^I}{2\pi}(z-\frac{d_I}{2})\int_0^{2\pi}\int_{r_i}^{r_o} \frac{r_c}{R_1^3}\cos(p_I\theta_I)dr_c d\theta_I \tag{49}$$

The integral terms in (47)-(49) can be evaluated along the radial direction resulting in the need to numerically evaluate only one integral. For instance, the evaluation of (49) yields

$$B_z^I = \frac{1}{\pi}(z-\frac{d_I}{2})B_m^I\int_0^{2\pi}\left[\frac{r^2+(z-d_I/2)^2 - rr_o\cos(\theta-\theta_I)}{R_1(r_o,d_I/2)}\right.$$
$$\left.-\frac{r^2+(z-d_I/2)^2 - rr_i\cos(\theta-\theta_I)}{R_1(r_i,d_I/2)}\right]\frac{\cos(p_I\theta_I)}{N(\theta,\theta_I,z,d_I/2)}d\theta_I \tag{50}$$

where

$$N(\theta,\theta_I z,z_I) = [r^2\cos(2(\theta-\theta_I)) - r^2 - 2(z-z_I)^2] \tag{51}$$

Similarly substituting (46) into (39) the magnetic scalar potential is

$$\phi(r,\theta,z) = \frac{2B_m^I}{4\pi\mu_0}\int_0^{2\pi}\int_{r_i}^{r_o}\frac{\cos(p_I\theta_I)}{R_1(r_c,d_I/2)}r_c dr_c d\theta_I \tag{52}$$

Evaluating (52) along the radial direction yields:

$$\phi^I(r,\theta,z) = \frac{B_m^I}{2\pi\mu_0}\int_0^{2\pi}\{\cos(p_I\theta_I)[R_1(r_o,d_I/2) - R_1(r_i,d_I/2)]$$
$$+ r\cos(\theta-\theta_I)\frac{\log[r_o - r\cos(\theta-\theta_I) + R_1(r_o,d_I/2)]}{\log[r_i - r\cos(\theta-\theta_I) + R_1(r_i,d_I/2)]}\}d\theta_I \tag{53}$$

Defining a new integration variable:

$$\theta_d = \theta - \theta_I \tag{54}$$

allows (53) to be written as:

$$\phi^I(r,\theta,z) = B_m^I\int_0^{2\pi}\frac{\cos[p_I(\theta-\theta_d)}{2\pi\mu_0}][R_2(r_i,d_I/2) - R_2(r_o,d_I/2)]d\theta_d$$
$$+\frac{B_m^I r}{2\pi\mu_0}\int_0^{2\pi}\cos[(p_I(\theta-\theta_d)]\cos(\theta_d)$$
$$\times\log\left[\frac{r_i - r\cos(\theta_d) + R_2(r_i,d_I/2)}{r_o - r\cos(\theta_d) + R_2(r_o,d_I/2)}\right]d\theta_d \tag{55}$$

where:

$$R_2(r_c,z_I) = \sqrt{r^2 + r_c^2 - 2rr_c\cos(\theta_d) + (z-z_I)^2} \tag{56}$$

IV. Magnetic Field Validation

The analytical magnetic flux density equations were compared with the field computed using a 3-D JMAG FEA model and a magnetic charge sheet model developed in COMSOL. The parameters for the axial rotor are shown in TABLE I. The flux density was compared at $(r,z) = (24.5,20)$ mm. The Simpson's rule was used to calculate the integral terms. The comparison is shown in Fig. 6 and Fig. 7. It can be seen that good agreement was achieved between the analytic and numerical models. The significant field changes with respect to radial position are clearly apparent when looking at the field plots shown in Fig. 8 - Fig. 11.

TABLE I
AXIAL ROTOR PARAMETERS

Description	Value	Unit
Outer radius, r_o	30	mm
Inner radius, r_i	20	mm
Axial length, d_I	30	mm
Pole pairs, $p_I = p$	4	-
Magnetic permeability, μ_r	1.05	-
Remnant flux density, B_r	1.27	T
Density of magnet material	7600	kg/m^3

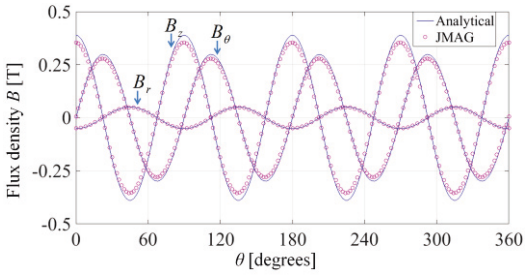

Fig. 6. Magnetic flux density comparison between the analytical model and 3-D JMAG model.

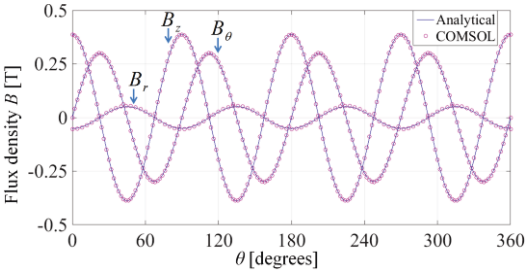

Fig. 7. Magnetic flux density comparison between the analytical model and COMSOL charge sheet FEA model.

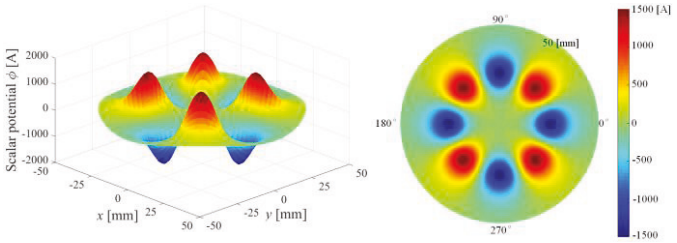

(a) (b)

Fig. 8. (a) Surface and (b) contour plot for the scalar potential function evaluated at $z = 20$ mm.

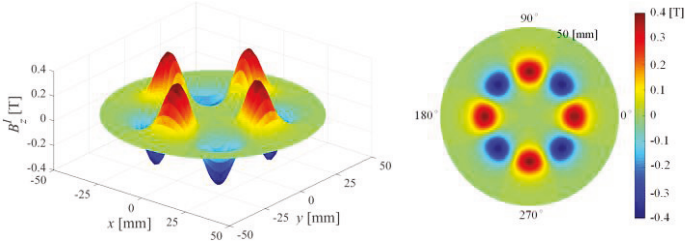

(a) (b)

Fig. 9. (a) Surface and (b) contour plot for the B_z magnetic field component evaluated at $z = 20$ mm.

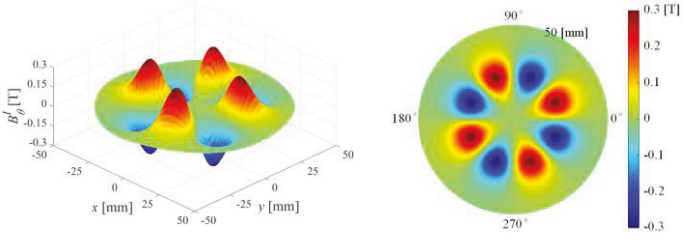

(a) (b)

Fig. 10. (a) Surface and (b) contour plot for the B_θ magnetic field component evaluated at $z = 20$ mm.

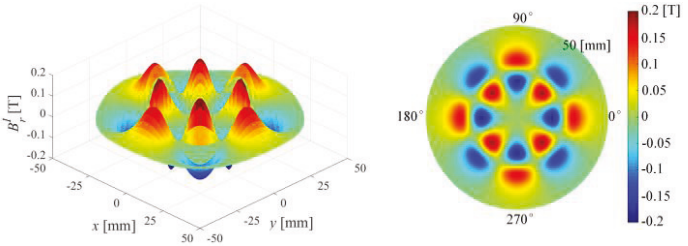

(a) (b)

Fig. 11. (a) Surface and (b) contour plot for the B_r magnetic field component evaluated at $z = 20$ mm.

V. Coupling Torque

Utilizing the equations given in the previous section one can compute the torque resulting from the interaction of two Halbach AMCs. Consider the problem shown in Fig. 12(a) in which a second axial Halbach rotor is placed above the first. The rotors are separated by a gap g. The two rotors have the same inner radius and outer radius. Rotor *II* has an axial length of d_{II} and p_{II} pole-pairs. In order to generate non-zero average torque the two rotors' pole-pairs are equal $p=p_I = p_{II}$.

In order to compute the torque, the two rotors are replaced with two fictitious magnetic charge discs, as shown in Fig. 12(b), that are axially located at $z_I = d_I/2$ and $z_{II}=d_I/2+g$. The magnetic charge function for rotor *II* is defined as

$$\rho_m^{II}(\theta) = 2B_m^{II}\cos[p(\theta-\theta_t)] \tag{57}$$

where

$$B_m^{II} = 2c_1 B_r \frac{(\mu_r+1)e^{k_{II}}(e^{k_{II}}-e^{-k_{II}})}{e^{2k_{II}}(\mu_r+1)^2 - e^{-2k_{II}}(\mu_r-1)^2} \tag{58}$$

$$k_{II} = p\frac{d_{II}}{r_o+r_i} \tag{59}$$

and θ_t is an initial angular position of the field on disc *II*.

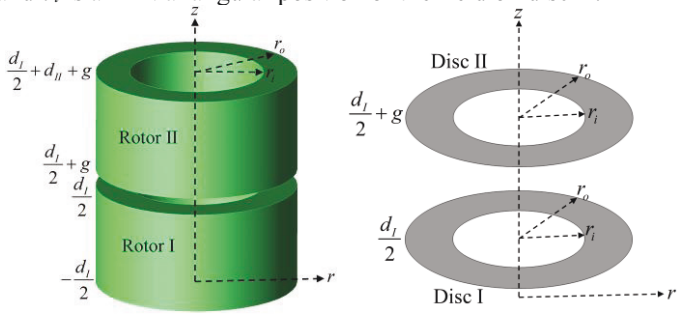

(a) (b)

Fig. 12. (a) The model of a Halbach axial magnetic coupling separated by gap g and (b) the equivalent fictitious magnetic charge disc model.

The magnetic energy contained within the problem region can be computed from [22]

$$W = \int_0^{2\pi}\int_{r_i}^{r_o}\phi^I(r,\theta,z_{II})\rho_m^{II}(\theta)rdrd\theta \tag{60}$$

where ϕ^I is defined in (55). The torque on the surface of rotor *II* can then be calculated from the magnetic energy by [22]

$$T = \left.\frac{\partial W}{\partial\theta}\right|_{\phi^I=\text{constant}} \tag{61}$$

Substituting (60) into (61) one obtains

$$T = \int_0^{2\pi}\int_{r_i}^{r_o}\phi^I(r,\theta,z_{II})\frac{\partial\rho_m^{II}(\theta)}{\partial\theta}rdrd\theta \tag{62}$$

Then substituting (55) and (57) into (62) and evaluating the integral with respect to θ one obtains

$$T(\theta_t) = \sin(p\theta_t)\frac{B_m^I B_m^{II}}{\mu_0}p\int_0^{2\pi}\int_{r_i}^{r_o}\cos(p\theta_d)R_3(r,\theta_d) + \cos(p\theta_d)\cos(\theta_d)\log[R_4(r,\theta_d)]r^2drd\theta_d \tag{63}$$

where

$$R_3(r,\theta_d) = \sqrt{r_o^2+r^2+g^2-2rr_o\cos(\theta_d)} - \sqrt{r_i^2+r^2+g^2-2rr_i\cos(\theta_d)} \tag{64}$$

$$R_4(r,\theta_d) = \frac{r_o - r\cos(\theta_d)+\sqrt{r_o^2+r^2+g^2-2rr_o\cos(\theta_d)}}{r_i - r\cos(\theta_d)+\sqrt{r_i^2+r^2+g^2-2rr_i\cos(\theta_d)}} \tag{65}$$

The radial integral term in (63) can be evaluated but its solution is too long to be included in this paper.

VI. Torque Validation

The parameters used to model each axial rotor are the same and are given in Table I. The torque obtained from (63) is calculated as a function of θ_t and compared with the 3-D JMAG model and COMSOL charge sheet FEA model when the air-gap g=1mm is used. The comparison is shown in Fig. 13. The discrepancy at the peak value between the analytical

and JMAG model is within 2% and the discrepancy between the analytical model and COMSOL is within 0.02%.

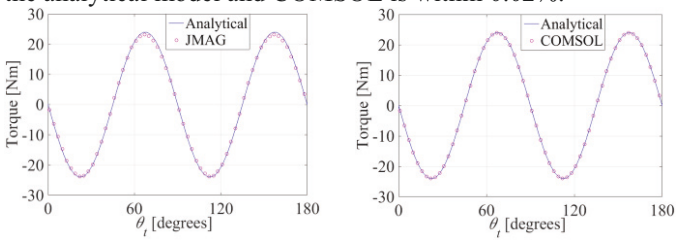

(a) (b)

Fig. 13. Torque comparison between (a) the analytical model and 3-D JMAG model and (b) the analytical model and the COMSOL charge sheet model.

VII. Parameter Analysis

Using the parameters shown in Table I, the axial length of the two rotors, d_{I} and d_{II} were both varied while keeping other parameters constant. The calculated results are shown in Fig. 14, it can be seen that the maximum mass torque density occurs when the axial length of the outer and inner rotors are equal. Therefore, in the following analysis $d_{\mathrm{I}} = d_{\mathrm{II}}$.

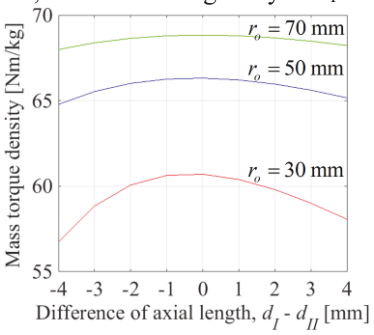

Fig. 14. Mass torque density with different axial lengths.

With the outer radius r_o fixed, the inner radius r_i and axial length d were varied to obtain the maximum mass torque density and volumetric torque density. An example of the plot showing the maximum torque point for the case when r_o = 55 mm and p = 4 is shown in Fig. 15. It can be seen that the peak mass and volumetric torque density occur at different locations. The peak mass torque density occurs when (r_i,d) = (28,18) mm and peak volume torque density occurs at (r_i,d) = (0,18) mm

The peak mass and volumetric torque density for different outer radii and pole-pairs was calculated and the resulting plot for the case when g = 1 mm and for g = 10mm is shown in Fig. 16 and Fig. 17. Fig. 16 shows that extremely high torque densities can be created at a very small air-gap and the torque density keeps increasing as the number of pole-pairs increase At the small air gap the torque density is more dependent on pole-number than outer radius. In contrast, Fig. 17 shows that with an increased air-gap the outer radius has a bigger impact on torque density and the increased pole number decreases torque density (due to the larger flux leakage).

Defining the radius ratio

$$\Gamma = r_i / r_o \tag{66}$$

the value of Γ as a function of pole-pair and outer radius that yields the peak mass torque density for g = 1 mm and g = 10 mm was computed. The resulting values are shown in Fig. 18. It can be seen that Γ is not a constant ratio as some have stated in the past.

Using a Dell PowerEdge T410 the calculation time for the analytic based and numerical models are compared in Table II.

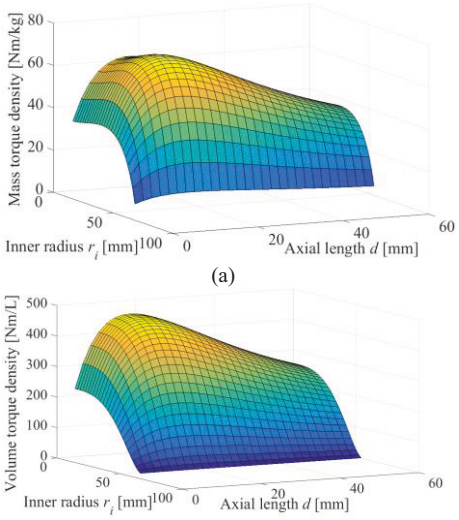

(a) (b)

Fig. 15. (a) Mass torque density and (b) volumetric torque density as a function of axial length and inner radius when r_o = 55mm, g = 1mm, p = 4.

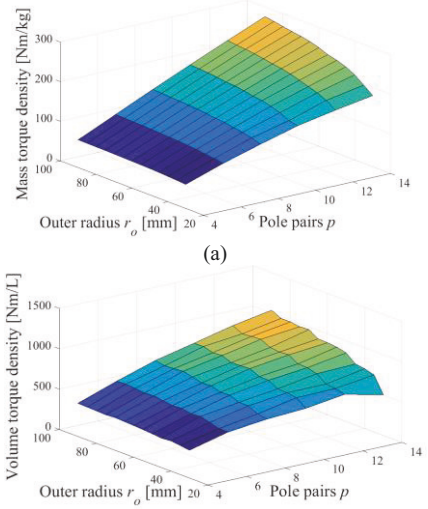

(a) (b)

Fig. 16. (a) Peak mass torque density and (b) volumetric torque density as a function of outer radius r_o and pole pairs when g = 1 mm.

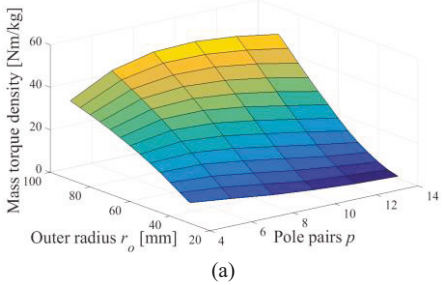

(a)

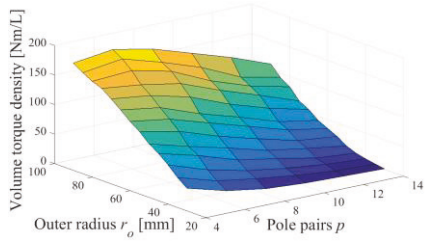

(b)

Fig. 17. (a) Peak mass torque density and (b) volumetric torque density as a function of outer radius r_o and pole pairs when g = 10 mm.

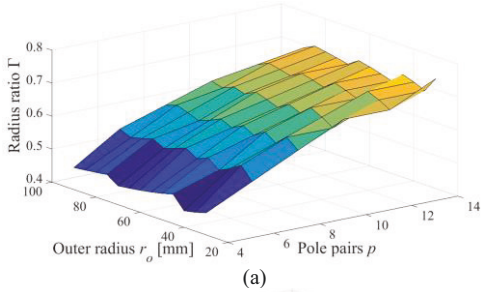

(a)

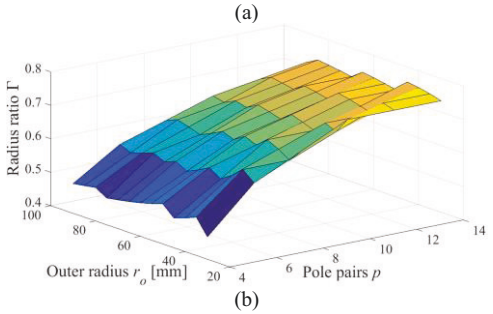

(b)

Fig. 18. Radius ratio for achieving peak mass torque as a function of outer radius r_o and pole pairs when (a) g = 1 mm and (b) g = 10 mm.

TABLE II
RUN-TIME FOR TORQUE CALCULATION

Description	Analytical	JMAG	COMSOL	Unit
Run-time	3	252	143	s

VIII. CONCLUSION

This paper has presented a new technique for computing the torque and fields for an AMC. The approach was demonstrated for a Halbach rotor coupling. The benefit of using the presented approach lies in the ability to accurately derive the 3-D field and torque equations from the magnitude of the field determined from a 2-D solution. A very good agreement was achieved between the analytical and FEA models. It was also shown that when the AMC air-gap is small, the pole-pairs have a larger influence on the torque density. While when the AMC air gap is large, the outer radius has a more dominant influence on torque.

ACKNOWLEDGMENT

The authors would gratefully like to thank the JMAG corporations for the use of their FEA software. This material is based upon work partially supported by the National Science Foundation under Grant No. 1408310 as well as a North Carolina Ocean Energy Grant.

REFERENCES

[1] G. S. Highfill and L. A. Halverson, "Lowering total cost of ownership with breakthrough magnetic torque transfer technology," in *IEEE Cement Ind. Tech. Conf.*, 2006.
[2] R. Montague, C. Bingham, and K. Atallah, "Servo Control of Magnetic Gears," *IEEE/ASME Trans on Mech.* vol. 17, no. 2, pp. 269-278, 2012.
[3] E. P. Furlani, *Permanent magnet and electromechnaical devices materials, analysis, and applications*. San Diego: Academic Press, 2001.
[4] P. O. Rasmussen, T. O. Andersen, F. T. Jorgensen, and O. Nielsen, "Development of a high-performance magnetic gear," *IEEE Trans. Ind. Appl.*, vol. 41, no. 3, pp. 764-770, 2005.
[5] V. M. Acharya, M. D. Calvin, and J. Z. Bird, "A low torque ripple flux focusing axial magnetic gear," presented at the 7th IET Inter. Conf. Power Elect. Mach. Drives, Manchester, UK, 2014.
[6] J. P. Yonnet, "A new type of permanent magnet coupling," *IEEE Trans. Magn.*, vol. 17, no. 6, pp. 2991-2993, 1981.
[7] T. Lubin, S. Mezani, and A. Rezzoug, "Simple Analytical Expressions for the Force and Torque of Axial Magnetic Couplings," *IEEE Trans. Energy Conv.*, vol. 27, no. 2, pp. 536-546, 2012.
[8] T. Lubin, S. Mezani, and A. Rezzoug, "Experimental and Theoretical Analyses of Axial Magnetic Coupling Under Steady-State and Transient Operations," *IEEE Trans. Ind. Elect.*, vol. 61, no. 8, pp. 4356-4365, 2014.
[9] R. Wang, E. P. Furlani, and Z. J. Cendes, "Design and analysis of a permanent magnet axial coupling using 3D finite element field computations," *IEEE Trans. Magn.*, vol. 30, no. 4, pp. 2292-2295, 1994.
[10] H. Shin, J. Choi, S. Jang, and K. Lim, "Design and Analysis of Axial Permanent Magnet<newline/> Couplings Based on 3D FEM," *IEEE Trans. Magn.*, vol. 49, no. 7, pp. 3985-3988, 2013.
[11] Y. Yeong-Der, G. Chiou, x, Ji, D.-R. Huang, and W. Shyh-Jier, "Theoretical computations for the torque of magnetic coupling," *IEEE Trans. Magn.*, vol. 31, no. 3, pp. 1881-1884, 1995.
[12] B. Dolisy, S. Mezani, T. Lubin, and J. Leveque, "A New Analytical Torque Formula for Axial Field Permanent Magnets Coupling," *IEEE Trans. Energy Conv.* , vol. 30, no. 3, pp. 892-899, 2015.
[13] B. Dolisy, T. Lubin, S. Mezani, and J. Leveque, "Three-dimensional analytical model for an axial-field magnetic coupling," *Prog. Electromag. Res. M*, vol. 35, no. pp. 173-182, 2014.
[14] E. P. Furlani, "Formulas for the force and torque of axial couplings," *IEEE Trans. Magn.* , vol. 29, no. 5, pp. 2295-2301, 1993.
[15] R. Waring, J. Hall, K. Pullen, and M. R. Etemad, "An investigation of face type magnetic couplers," *Proc. Instn. Mech. Engrs. Part A*, vol. 210, no. pp. 263-272, 1996.
[16] D. J. Eichenberg, C. A. Gallo, and W. K. Thompson, "Development and Testing of an Axial Halbach Magnetic Bearing," NASA, Report # TM—2006-214357, Cleveland, OH, July 2006.
[17] W. K. Thompson, "Three-Dimensional Field Solutions for Multi-Pole Cylinderical Halbach Array in an Axial Orientation," Report # NASA/TM—2006-214359, Cleveland, OH,, Sept. 2006.
[18] C. A. Balanis, *Advanced Engineering Electromagnetics*: John Wiley & Sons, 1989.
[19] Z. P. Xia, Z. Q. Zhu, and D. Howe, "Analytical magnetic field analysis of Halbach magnetized permanent-magnet machines," *IEEE Trans. Magn.*, vol. 40, no. 4, pp. 1864-1872, 2004.
[20] D. J. Griffiths, *Introduction to Electrodynamics*. New Jersey: Prentice Hall, 1999.
[21] J. P. Selvaggi, S. Salon, O. M. Kwon, M. V. K. Chari, and M. DeBortoli, "Computation of the External Magnetic Field, Near-Field or Far-Field, From a Circular Cylindrical Magnetic Source Using Toroidal Functions," *IEEE Trans. Magn.*, vol. 43, no. 4, pp. 1153-1156, 2007.
[22] O. D. Jefimenko, *Electricity and Magnetism*. New York: Meredith Publishing Co., 1966.